

Non-Gaussianity of the Cosmic Infrared Background anisotropies II : Predictions of the bispectrum and constraints forecast

A. Pénin¹ ^{*}, F. Lacasa² and N. Aghanim²

¹ Aix Marseille Université, CNRS, LAM (Laboratoire d'Astrophysique de Marseille) UMR 7326, 13388, Marseille, France

² Institut d'Astrophysique Spatiale (IAS), Bâtiment 121, F-91405 Orsay (France); Université Paris-Sud 11 and CNRS (UMR 8617)

Accepted 0000. Received 0000

ABSTRACT

Using a full analytical computation of the bispectrum based on the halo model together with the halo occupation number, we derive the bispectrum of the cosmic infrared background (CIB) anisotropies that trace the clustering of dusty-star-forming galaxies. We focus our analysis on wavelengths in the far-infrared and the sub-millimeter typical of the *Planck*/HFI and *Herschel*/SPIRE instruments, 350, 550, 850, and 1380 μm . We explore the bispectrum behaviour as a function of several models of evolution of galaxies and show that it is strongly sensitive to that ingredient. Contrary to the power spectrum, the bispectrum, at the four wavelengths, seems dominated by low redshift galaxies. Such a contribution can be hardly limited by applying low flux cuts. We also discuss the contributions of halo mass as a function of the redshift and the wavelength, recovering that each term is sensitive to a different mass range. Furthermore, we show that the CIB bispectrum is a strong contaminant of the Cosmic Microwave Background bispectrum at 850 μm and higher. Finally, a Fisher analysis of the power spectrum, bispectrum alone and of the combination of both shows that degeneracies on the HOD parameters are broken by including the bispectrum information, leading to tight constraints even when including foreground residuals.

Key words: Infrared : galaxies - Cosmology : large scale structure of the Universe - galaxies: statistics

1 INTRODUCTION

Observations in the far-Infrared (FIR) and in the sub-millimeter range are limited by confusion effects. Extragalactic sources below the detection limit lead to brightness fluctuations, because of the low resolution of the instruments. The resulting Cosmic Infrared Background (CIB) contains the radiation emitted by dusty star-forming galaxies (DSFG) since the decoupling. These galaxies have very high star formation rates (SFR) and are thus the main locations of star formation in the Universe. Most of their energy ($\sim 95\%$) is emitted in the IR as dust reprocesses and re-emits UV starlight in the IR. Only 15 % of the CIB is directly resolved into sources by *Herschel*/SPIRE at 250 μm (Oliver et al. 2010) and this fraction decreases with increasing wavelength. Statistical methods that permit to reach fluxes much lower than the confusion limit, for instance stacking, en-

able to increase the fraction of resolved CIB to 73 % at 250 μm with *Herschel*/SPIRE (Béthermin et al. 2012b). The unresolved sources thus give access to the majority of the DSFG emission. The CIB displays anisotropies that are the consequence of the underlying spatial distribution of DSFG. These anisotropies further probe the clustering of DSFG and the link between galaxies and dark matter halos in the large scale structure. The redshift distribution of the sources constituting the CIB shifts towards higher redshifts as the wavelength increases (Fernandez-Conde et al. 2008). As a result, a multi-wavelength study of the CIB gives, in principle, access to the redshift evolution of the anisotropies, and therefore to the evolution of the underlying population of galaxies.

The CIB anisotropies have been measured in the last few years over a wide range of scales and wavelengths from 100 μm to 1380 μm . They first have been detected at 160 μm (Lagache et al. 2007) and in *BLAST* data from 250 to 500 μm (Viero et al. 2009). Several measurements have fol-

^{*} E-mail: aurelie.penin@oamp.fr (AVR)

lowed in the submillimeter range (Hall et al. 2010; Fowler & Atacama Cosmology Telescope Team 2010). More recently, they have been measured in *Herschel*/SPIRE data at 250, 350, and 500 μm (Amblard et al. 2011; Viero et al. 2012) and in *Planck* data from 350 to 1380 μm (Planck Collaboration et al. 2011a) with unprecedented accuracy. At lower wavelengths, the main limitation of a CIB measurement is the contamination by Galactic cirrus on large angular scales (Planck Collaboration et al. 2011a). Pénin et al. (2012) measured the CIB power spectra at 100 and 160 μm by accurately removing this component using an independent tracer of dust, namely neutral hydrogen. It enabled the authors to extend the range of scales of the CIB measurement.

In parallel to the measurement of CIB, theoretical modeling has been the subject of a lot of activities. A biased linear power spectrum was fit to the data (Lagache et al. 2007; Hall et al. 2010), but a such a simple model has been ruled out by Planck Collaboration et al. (2011a). More complex models of clustering dedicated to DSFG were developed and used to analyse the data. They combine two different models: one for the evolution of galaxies and one for the distribution of dark matter. Concerning the former, several recent models, parametric or physically motivated, that reproduce well current measurements of differential number counts and luminosity functions have been used (Lagache et al. 2004; Negrello et al. 2007; Béthermin et al. 2011).

For the distribution of galaxies versus dark matter, the halo model (Cooray & Sheth 2002) has been applied to DSFG. It describes the spatial distribution of dark matter halos. The introduction of the halo occupation distribution (HOD) allows to extend this framework to the distribution of galaxies by prescribing the number of galaxies within a halo as a function of the halo mass. This analytical approach has been widely applied and used to study the CIB power spectrum (Viero et al. 2009; Pénin et al. 2012; Xia et al. 2012).

Being a fully analytical approach, the halo model can be extended to higher order correlations. The 3-point correlation function as well as its Fourier space analogue, the bispectrum, is the lowest order indicator of non-Gaussianity. First attempts at predicting the bispectrum in the millimetre domain have been made by Argüeso et al. (2003) considering the measured two-point correlation function of both DSFG and radio galaxies together. The first measurement of the bispectrum of extragalactic point sources in *WMAP1* data was performed by Komatsu et al. (2003). At that time the correlated anisotropies of the CIB had not been detected, only the Poisson component had (Lagache & Puget 2000; Lagache et al. 2007). Moreover, at the frequencies probed by *WMAP* (Bennett et al. 2003) the dominant extragalactic sources are radio-emitting galaxies. They are unclustered which makes the bispectrum a constant. The subject of bispectrum from extragalactic sources has recently gained interest both from the point of view of the modeling, in particular for the CIB contribution (Lacasa et al. 2012), and from the point of view of the measurement (Crawford et al. 2013). This regain of interest has mostly two motivations. First, the CIB bispectrum is a complementary information to the number counts, luminosity function and power spectrum that could help constraining models of clustering and evolution of DSFG galaxies. Second, the CIB is a foreground to the CMB measurement and its non-Gaussianity needs to be looked at carefully.

In this paper, we use the formalism developed in a companion paper Lacasa et al. (2013), referred to hereafter as Paper1, to compute predictions of the bispectrum of CIB anisotropies at far-infrared and millimeter wavelengths and to investigate the dependencies of the bispectrum, as a function of the wavelength. We summarize in Sect. 2 the formalism of the bispectrum, detailed in Paper1. We summarize how we derive the predictions and investigate the dependencies of the CIB bispectrum on the input models of galaxies in Sect. 3. We then investigate, in Sect. 4, the mass and redshift ranges of the dark matter halos in which DSFG are embedded and which contribute to the CIB bispectrum. We present the effect of the emissivity flux cuts in Sect. 5. Eventually, we compare the CIB bispectrum to that of the CMB in Sect. 6 and we carry a Fisher analysis to investigate to which extent combined data of power spectra and bispectra constrain the HOD parameters. Finally we conclude in Sect. 7.

2 FORMALISM OF THE BISPECTRUM

We summarize here the formalism of the power spectrum and the bispectrum of CIB anisotropies. Both require two main ingredients, the emissivities that rule the evolution of DSFG and the distribution of dark matter halos in which galaxies are embedded, described by the halo model. We will introduce the halo occupation number, that rules how galaxies populate halos.

2.1 The angular power spectrum

Following Haiman & Knox (2000), Knox et al. (2001), Pénin et al. (2012), and using the Limber approximation, the angular power spectrum of the CIB anisotropies at a given wavelength λ is:

$$C_\ell^\lambda = \int \frac{dz}{r^2} \frac{dr}{dz} a^2(z) \bar{j}_\lambda^2(z) P_{\text{gal}}(k, z) + C_\ell^{\text{shot}} \quad (1)$$

where r is the comoving distance and $a(z) = (1+z)^{-1}$ is the scale factor. $\bar{j}_\lambda(z)$ is the mean emissivity of DSFG given by a model of evolution of galaxies (see Sect 2.5.1). $P_{\text{gal}}(k, z)$ is the galaxy 3D power spectrum derived from the halo model. C_ℓ^{shot} is the shot-noise contribution described in Sect.2.3.2.

2.2 The angular bispectrum

As derived in Paper1, in the Limber approximation the bispectrum of the CIB anisotropies at a given wavelength λ is

$$b_{\ell_1 \ell_2 \ell_3}^\lambda = \int \frac{dz}{r^4} \frac{dr}{dz} a^3(z) \bar{j}_\lambda^3(z) B_{\text{gal}}^{\text{clus}}(k_{123}, z) + b_{\ell_1 \ell_2 \ell_3}^{\text{shot}} \quad (2)$$

where $B_{\text{gal}}(k_{123}, z)$ is the galaxy 3D bispectrum derived in the framework of the halo model, and $b_{\ell_1 \ell_2 \ell_3}^{\text{shot}}$ is described in Sect.2.3.2. For clarity, we write (k_1, k_2, k_3) as k_{123} in the following.

2.3 The 3D bispectrum from the halo model

Similarly to the 3D power spectrum, the 3D bispectrum has both clustering and the shot-noise contributions (see Paper1 for details):

$$B_{\text{gal}}(k_{123}, z) = B_{\text{gal}}^{\text{clus}}(k_{123}, z) + B_{\text{gal}}^{\text{shot}}(k_{123}, z) \quad (3)$$

2.3.1 The clustering terms

In the framework of the halo model, the bispectrum can be written as the sum of three components, 1-halo, 2-halo and 3-halo terms:

$$B_{\text{gal}}^{\text{clus}}(k_{123}, z) = B_{\text{gal}}^{\text{1h}}(k_{123}, z) + B_{\text{gal}}^{\text{2h}}(k_{123}, z) + B_{\text{gal}}^{\text{3h}}(k_{123}, z) \quad (4)$$

The 1-halo term is the contribution of three galaxies within the same halo and it dominates at small spatial scales. The 2-halo term is the case of two galaxies within one halo and a third galaxy in another halo. It mainly contributes at intermediate spatial scales. Finally, the 3-halo term is the contribution of three galaxies in three distinct halos and dominates at large spatial scales.

The 1-halo term of the bispectrum reads :

$$B_{\text{gal}}^{\text{1h}}(k_{123}, z) = \int dM \frac{\langle N_{\text{gal}}(N_{\text{gal}} - 1)(N_{\text{gal}} - 2) \rangle}{\bar{n}_{\text{gal}}^3} \frac{dN_h}{dM} \quad (5)$$

$$\times |u(k_1|M) u(k_2|M) u(k_3|M)| \quad (6)$$

where dN_h/dM is the halo mass function, $u(k|M)$ is the normalized Fourier transform of the halo density profile, and $\langle N_{\text{gal}} \rangle$ is the probability of having N_{gal} galaxies in a halo of mass M . The latter is described by the halo occupation distribution (Kravtsov et al. 2004). Finally, \bar{n}_{gal} is the mean number of galaxies given by:

$$\bar{n}_{\text{gal}} = \int dM \frac{dN_h}{dM} \langle N_{\text{gal}} \rangle \quad (7)$$

In the following, we use the mass function of Sheth & Tormen (1999), the Navarro et al. (1996) halo density profile, and the HOD is described in more details in Sect 2.4.

In order to simplify the equations for the 2- and 3-halo terms, we introduce the following notations

$$\mathcal{F}_1(k, z) = \int dM \frac{\langle N_{\text{gal}}(M) \rangle}{\bar{n}_{\text{gal}}(z)} \frac{dN_h}{dM} b_1(M) |u(k|M)| \quad (8)$$

$$\mathcal{F}_2(k, z) = \int dM \frac{\langle N_{\text{gal}}(M) \rangle}{\bar{n}_{\text{gal}}(z)} \frac{dN_h}{dM} b_2(M) |u(k|M)| \quad (9)$$

$$\mathcal{G}_1(k_1, k_2, z) = \int dM \frac{\langle N_{\text{gal}}(N_{\text{gal}} - 1) \rangle}{\bar{n}_{\text{gal}}(z)^2} \frac{dN_h}{dM} b_1(M) \times |u(k_1|M) u(k_2|M)| \quad (10)$$

where $b_1(M)$ and $b_2(M)$ are respectively the first and second order halo biases associated to the chosen mass function.

The 2-halo term becomes:

$$B_{\text{gal}}^{\text{2h}}(k_{123}, z) = \mathcal{G}_1(k_1, k_2, z) P_{\text{lin}}(k_3, z) \mathcal{F}_1(k_3, z) + \mathcal{G}_1(k_1, k_3, z) P_{\text{lin}}(k_2, z) \mathcal{F}_1(k_2, z) + \mathcal{G}_1(k_2, k_3, z) P_{\text{lin}}(k_1, z) \mathcal{F}_1(k_1, z) \quad (11)$$

and the 3-halo term writes:

$$B_{\text{gal}}^{\text{3h}}(k_{123}, z) = \mathcal{F}_1(k_1, z) \mathcal{F}_1(k_2, z) \mathcal{F}_1(k_3, z) \times [F_{12}^s(k_1, k_2) P_{\text{lin}}(k_1, z) P_{\text{lin}}(k_2, z) + \text{perm.}] \quad (12)$$

$$+ \mathcal{F}_1(k_1, z) \mathcal{F}_1(k_2, z) \mathcal{F}_2(k_3, z) \times P_{\text{lin}}(k_1, z) P_{\text{lin}}(k_2, z) + \mathcal{F}_1(k_1, z) \mathcal{F}_2(k_2, z) \mathcal{F}_1(k_3, z) \times P_{\text{lin}}(k_1, z) P_{\text{lin}}(k_3, z) + \mathcal{F}_2(k_1, z) \mathcal{F}_1(k_2, z) \mathcal{F}_1(k_3, z) \times P_{\text{lin}}(k_2, z) P_{\text{lin}}(k_3, z)$$

where $P_{\text{lin}}(k, z)$ is the linear power spectrum, and $F_{\alpha\beta}^s$ is the kernel due to the non-linearity of gravity at second-order in perturbation theory (Fry 1984; Gil-Marín et al. 2012):

$$F_{\alpha\beta}^s = \frac{2k_\gamma^4 - 3(k_\alpha^4 + k_\beta^4) + 3k_\gamma^2(k_\alpha^2 + k_\beta^2) + 10k_\alpha^2 k_\beta^2}{28k_\alpha^2 k_\beta^2} \quad (13)$$

with γ the third index.

2.3.2 The shot noise terms

In the case of the power spectrum, there is only one shot noise term that depends on the differential number counts and the flux cut S_{cut} . Thus, it is independent of the HOD:

$$C_\ell^{\text{shot}} = \int_0^{S_{\text{cut}}} S^2 \frac{dN}{dS} dS \quad (14)$$

The shot noise term of the bispectrum has two components.

$$b_{\ell_1 \ell_2 \ell_3}^{\text{shot}} = b_{\ell_1 \ell_2 \ell_3}^{\text{shot1g}} + b_{\ell_1 \ell_2 \ell_3}^{\text{shot2g}} \quad (15)$$

The 1-galaxy term is the correlation of one galaxy with itself three times and the 2-galaxy term is the correlation of one galaxy with itself and with another one (within the same halo or not). Similarly to the power spectrum, the 1-galaxy term is written:

$$b_{\ell_1 \ell_2 \ell_3}^{\text{shot1g}} = \int_0^{S_{\text{cut}}} S^3 \frac{dN}{dS} dS \quad (16)$$

$$= \int dz \frac{dr}{dz} a^3(z) j^{(3)}(z) \quad (17)$$

where $j^{(n)}$ is the n-th order emissivity:

$$j^{(n)}(z) = \frac{(1+z)^n}{\frac{dr}{dz}} \int_0^{S_{\text{cut}}} S^n \frac{d^2 N}{dS dz} dS \quad (18)$$

The 2-galaxy shot noise term is:

$$b_{\ell_1 \ell_2 \ell_3}^{\text{shot2g}} = \int \frac{dz}{r^4} \frac{dr}{dz} a^3(z) j^{(1)}(z) j^{(2)}(z) \quad (19)$$

$$\times [P_{\text{gal}}(k_1) + P_{\text{gal}}(k_2) + P_{\text{gal}}(k_3)] \quad (20)$$

where $P_{\text{gal}}(k)$ is the 3D power spectrum derived from the halo model. Thus this term depends on the HOD.

2.4 The halo occupation distribution

The standard halo occupation distribution rules the number of galaxies in a halo as a function of the halo mass only (Kravtsov et al. 2004; Tinker & Wetzel 2010). In such a framework, the distribution of galaxies within a halo is Poissonian. Simulations, as well as recent data suggest a necessary distinction between the major galaxy that lies in the centre of the halo and the satellite galaxies that populate the rest of the halo (Berlind & Weinberg 2002; Kravtsov et al. 2004; Zheng et al. 2005; van den Bosch et al. 2007). Thus

$$\langle N_{\text{gal}} \rangle = \langle N_{\text{cen}} \rangle + \langle N_{\text{sat}} \rangle \quad (21)$$

According to the prescription of Tinker & Wetzel (2010), the occupation function of central galaxies is

$$\langle N_{\text{cen}} \rangle = \frac{1}{2} \left[1 + \operatorname{erf} \left(\frac{\log M - \log M_{\text{min}}}{\sigma_{\log M}} \right) \right] \quad (22)$$

where M_{min} is the halo mass at which a halo has a 50% probability of hosting a central galaxy and $\sigma_{\log M}$ controls the width of the transition between zero and one central galaxy. There is a smooth transition between low-mass halos that do not contain bright enough galaxies ($M \ll M_{\text{min}}$) and more massive halos that always contain a bright central galaxy ($M \gg M_{\text{min}}$). The satellite occupation function is

$$\langle N_{\text{sat}} \rangle = \frac{1}{2} \left[1 + \operatorname{erf} \left(\frac{\log M - \log 2M_{\text{min}}}{\sigma_{\log M}} \right) \right] \left(\frac{M}{M_{\text{sat}}} \right)^{\alpha_{\text{sat}}}. \quad (23)$$

It has a cut-off of the same form as the central occupation with a transition mass that is twice higher than that of the central galaxies. This is made to prevent halos having a low probability of hosting a central galaxy to contain satellite galaxies. The number of satellite galaxies grows with a slope α_{sat} . Making use of the HOD, the angular power spectrum and bispectrum of CIB anisotropies depend on four halo model parameters: α_{sat} , M_{min} , M_{sat} , and $\sigma_{\log M}$.

The halo model formalism has only been applied to DSFG in the last few years but it has been extensively and successfully used to reproduce the clustering of optically selected galaxies and studied on simulations (Cooray et al. 2010; Tinker et al. 2010; Coupon et al. 2012). Even if numerical hydrodynamical simulations as well as semi-analytic models predict that α_{sat} equals one (Kravtsov et al. 2004; Gao et al. 2004; Zheng et al. 2005; Croton et al. 2006), measurements are not so unambiguous. α_{sat} tends to be higher than one for DSFG but no convergence on its value is achieved yet. Cooray et al. (2010) computed the correlation function of the sources detected in **Herschel**/SPIRE data at 250, 350, and 500 μm and α_{sat} was found to range between 1.3 and > 1.8 . Concerning unresolved sources, results from **Herschel**/SPIRE (Amblard et al. 2011) and **Planck** (Planck Collaboration et al. 2011a) lead to values between 0.96 and 1.8 depending on the wavelength. More recently, Xia et al. (2012) succeeded in fitting **Planck**, **Herschel**/SPIRE and the **South Pole Telescope** data from 250 μm to 1.3 mm by one single model, and obtained $\alpha_{\text{sat}} = 1.81 \pm 0.04$.

Both M_{min} and M_{sat} are hardly constrained separately as they are highly degenerate when dealing with CIB anisotropies power spectra (Pénin et al. 2012). Therefore, one parameter is usually fixed whereas the other is derived from the data (Planck Collaboration et al. 2011a; Xia et al. 2012) as inspired from theoretical studies and semi-analytic models which expect $M_{\text{sat}} = 10\text{--}25M_{\text{min}}$. Planck Collaboration et al. (2011a) assumed $M_{\text{sat}} = 3.3 M_{\text{min}}$ and found values of $\log(M_{\text{min}}/M_{\odot})$ between 11.82 and 12.50.

2.5 The emissivities

We use three models of evolution of DSFG throughout this study and compare their output emissivities. These three models are based on different philosophies (semi-analytical, backward evolution) and all reproduce well current measurements but do predict different redshift evolution.

2.5.1 Models of evolution of galaxies

Several models of the evolution of DSFG have been proposed in the literature (Lapi et al. 2011; Gruppioni et al. 2011; Béthermin et al. 2011, 2012a). In the present study we focus on three models (Béthermin et al. 2011, 2012a; Negrello et al. 2007) all reproducing well observations (differential number counts, luminosity functions at several redshifts and differential number counts in redshift bins from **Herschel**). Their differences allow us to explore and compare the effects of the evolution of DSFG, in particular, on the bispectrum of the CIB anisotropies.

First, we consider an updated version of the model of Negrello et al. (2007) (hereafter **MODEL1**) that has been recently used by Xia et al. (2012) to model the power spectrum of the CIB anisotropies. This model uses two populations of galaxies, spirals at $z < 1.5$ and high- z sub-mm galaxies at $z > 1$. The latter are considered to be massive proto-spheroidal galaxies processing most of their stellar mass. Furthermore, the model assumes that star formation is triggered by the dark matter halo collapse/merger and is then controlled by self-regulated baryonic processes such as AGN feedback.

The second model (hereafter **MODEL2**), proposed by Béthermin et al. (2011), is a backward evolution model. It relies on a parametric luminosity function (LF) and a library of spectral energy distributions (SED) templates. The LF is taken to be a power law for low luminosities and a Gaussian for high luminosities. Béthermin et al. (2011) used the SED library of Lagache et al. (2004) which contains two different populations of galaxies: star-forming and late-type. The former emit over 95% of their energy in the IR while the latter emit half or less of their energy in the IR. **MODEL2** is described by thirteen free parameters. Best-fit parameters are computed using Monte-Carlo Markov Chains on available differential number counts and luminosity functions on a large range of IR wavelengths.

The third model (hereafter **MODEL3**), from Béthermin et al. (2012a), is an empirical model in which galaxies are split between main sequence (MS) galaxies and starburst (SB) ones. MS galaxies account for 85% of the star-formation density of the Universe at $z < 2$. The 15% left are due to SB galaxies which have high specific star-formation rates (sSFR), likely because of recent major mergers. In their model, Béthermin et al. (2012a) assume an SED that gets warmer with redshift for MS galaxies and a non-evolving SED for SB galaxies. Both SEDs are based on **Herschel** observations. The sSFR distribution is thus decomposed in the two modes, SB and MS. Following Sargent et al. (2012), the sSFR of MS galaxies vary with redshift and stellar mass whereas it remains constant for SB galaxies. The stellar mass function changes with the redshift as well. In addition, the model includes dust attenuation, AGN contribution and, magnification by strong lensing.

2.5.2 The emissivities

We derive the mean emissivities from the differential number counts as follows:

$$\bar{j}_{\lambda}(z) = (1+z) \int_0^{S_{\text{cut}}} S \frac{d^2 N}{dS dz} dS. \quad (24)$$

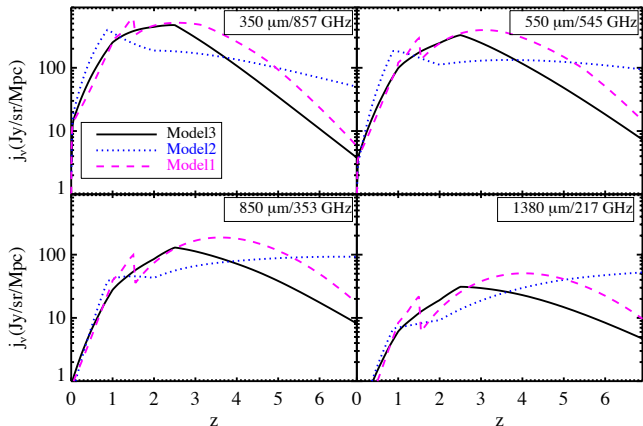


Figure 1. Emissivities for the three models of evolution of galaxies at long wavelengths used in the present study.

We display the emissivities at long wavelengths for the three models of evolution of galaxies in Fig. 1. The cut-offs at $z \sim 1$ and $z = 2$ of MODEL2 are due to the parametrisation of the luminosity function which has two breaks at these redshifts. The sharp break at $z = 1.5$ of MODEL1 is the result of the mix of two populations. The peak is caused by the contribution of starbursts galaxies.

The emissivities peak at different redshifts. The peak of the emissivity is shifted from $z \sim 1$ for MODEL2 to $z \sim 2.5$ for MODEL3, in better agreement with the peak of star formation rate in the Universe at $z \sim 2-3$ (Bouwens et al. 2012). MODEL3 also displays a peak at $z \sim 2$ at $350 \mu\text{m}$ that shifts up to $z \sim 4$. The three emissivities display a similar shape and amplitude up to $z \sim 1.5$. However, their behaviour is different at higher redshift. MODEL1 and MODEL3 emissivities peak at $z \sim 2-4$ for all the wavelengths whereas those of MODEL2 are either decreasing ($350 \mu\text{m}$) constant (550 and $850 \mu\text{m}$) or increasing ($1380 \mu\text{m}$). At very high redshifts ($z > 4$), MODEL1 and MODEL3 emissivities decrease whereas those of MODEL2 stay constant or increase. The behaviours of MODEL1 and MODEL3 are more in line with our recent knowledge of the evolution of the SFR with redshift (Bouwens et al. 2011). We therefore adopt MODEL3 as a baseline for the present study and we use the other models of evolution of galaxies to explore the range of possibilities for the bispectrum.

3 PREDICTIONS OF THE BISPECTRUM AND DEPENDENCIES ON THE MODELS OF EVOLUTION OF GALAXIES

We now review how the predictions of the bispectrum are computed and to what extent they depend on the emissivities. The latter are already known to have a strong influence on the shape and on the amplitude of the power spectrum (Pénin et al. 2012).

Planck Collaboration et al. (2011a) and Xia et al. (2012) derived sets of HOD parameters associated to their respective models of galaxies using the Tinker et al. (2008) mass function. However the second order bias, which is a key ingredient to compute the bispectrum, is not available for the

Tinker et al. (2008) mass function. We therefore make use of the Sheth & Tormen (1999) mass function and its associated first and second order biases. Consequently, we carry our fits of **Planck** power spectra for each wavelength and galaxy model under consideration. To this end, we fit the HOD parameters α_{sat} and M_{min} , fixing $M_{\text{sat}} = 10 M_{\text{min}}$ and $\sigma_{\log M} = 0.65$, at each wavelength, as HOD parameters are degenerate with the emissivity model. The fits are satisfactory, with reduced χ^2 ranging between 1 and 2. Best-fits values are given in Table. 1. Making use of the obtained best-fit HOD parameters, we compute the equilateral and squeezed bispectra at the four **Planck** wavelengths, 350 , 550 , 850 , and $1380 \mu\text{m}$. They are shown in Figs. 2 and 3. Lower panels display the ratio between bispectra with respect to that obtained with MODEL3. The difference does not depend much on the configuration but mainly on the wavelength and the scale. The ratio at ‘low’ wavelength between the bispectra of MODEL2 and MODEL3 is mainly lower than one. Regardless of the configuration, this ratio increases, and exceeds unity, with increasing wavelengths. The ratio between MODEL1 and MODEL3 stays below one between 550 and $1380 \mu\text{m}$. At $350 \mu\text{m}$, this ratio is above one and reaches three. It depends on the scale. Regardless of the configuration and the wavelength, there is always a scale range where bispectra differ by at least a factor two. The main differences are at low multipoles ($\ell < 300$). For instance, at $\ell = 100$, it varies between a factor nine for the equilateral at $550 \mu\text{m}$ and a factor 1.1 at $1380 \mu\text{m}$ for the squeezed configuration. At higher multipoles ($\ell > 1000$), the differences are smaller. At $\ell = 4000$, they are mostly around a factor 1-1.5 even if it reaches 2.7 for the equilateral at $850 \mu\text{m}$. These differences arise from the set of parameters of the HOD as well as from the model of galaxies.

Such differences in the predictions lead to a difference of the level of non-Gaussianity in the CIB anisotropies. By computing the ratio of the total bispectra for each model of galaxies we can get an insight on that level. MODEL2 predicts more non-Gaussianity than MODEL3 up to $850 \mu\text{m}$. The relative level predicted by MODEL1 varies with respect to the wavelength up to $850 \mu\text{m}$. At $1380 \mu\text{m}$, the amount of non-Gaussianity is similar with the three models of galaxies. Crawford et al. (2013) measured the amplitude of the bispectrum of the CIB at 220 GHz and $\ell = 2000$. They found $0.87 \pm 0.29 \pm 0.25 \mu\text{K}^3/\text{sr}$ (the first error is statistical and the second one is systematical) whereas we predict $3.86 \mu\text{K}^3/\text{sr}$ for MODEL3. One explanation for this disagreement could be that our predictions have been calibrated on power spectra with $\ell \in [200, 2000]$ whereas SPT is dedicated to higher multipoles.

Such behaviours show that fitting simultaneously power spectra and bispectra will lead to the exclusion of some models of evolution of galaxies that predict too much or not enough non-Gaussianity. We also note that the main differences are displayed at small multipoles ($\ell < 100$), therefore large CIB maps will be needed to be able to measure accurately the bispectrum on these scales. However, these scales are the most affected by Galactic dust and, at $1380 \mu\text{m}$ by CMB anisotropies (Planck Collaboration et al. 2013a). Nevertheless, we can expect that the combination of power spectra and bispectra measurements will allow to disentangle between models of evolution of galaxies.

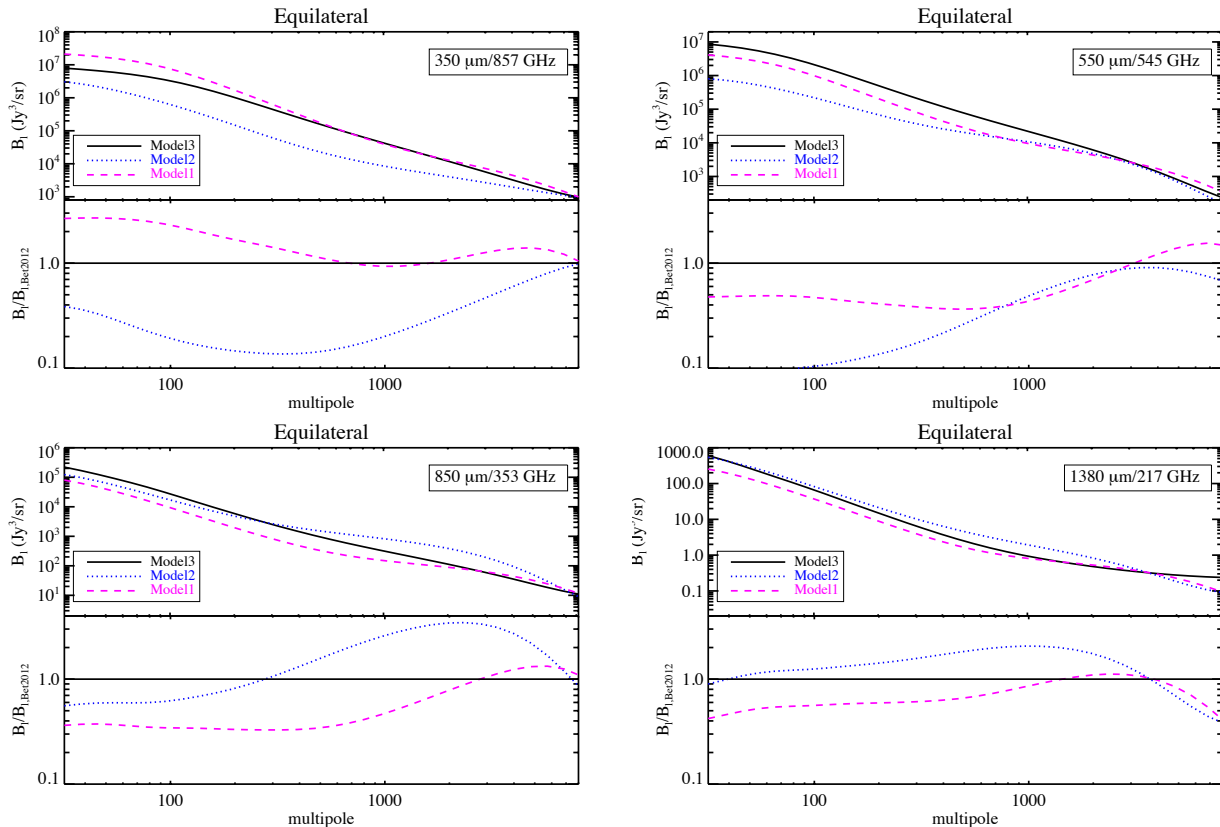


Figure 2. Top panels: Equilateral bispectra with the three models of evolution of galaxies. Lower panels: ratios between bispectra compared to the one computed with MODEL3.

Wavelength μm	Frequency GHz	parameters	MODEL1	MODEL2	MODEL3
350	857	α_{sat}	1.8	1.1	1.7
		$\log_{10} M_{\text{min}}$	12.8	12.6	12.8
550	545	α_{sat}	1.7	1.7	1.9
		$\log_{10} M_{\text{min}}$	12.2	12.8	12.6
850	353	α_{sat}	1.5	1.9	1.7
		$\log_{10} M_{\text{min}}$	11.6	12.6	12.2
1380	217	α_{sat}	1.4	1.6	1.5
		$\log_{10} M_{\text{min}}$	11.2	12.2	12

Table 1. Best-fits of the HOD parameters for PLANCK power spectra used to compute predictions of the bispectrum. We fixed $M_{\text{sat}} = 10M_{\text{min}}$ following Planck Collaboration et al. (2011a).

4 REDSHIFT AND HALO MASS CONTRIBUTIONS

We investigate the redshift contributions of the bispectrum compared to those of the power spectrum and eventually we explore the halo mass contribution as a function of the redshift.

4.1 Redshift contributions

One of the main unknown of the CIB is its redshift distribution. Recent measurements of differential number counts per redshift bins start to uncover its nature up to redshift 1.5 (Jauzac et al. 2011; Béthermin et al. 2012b). First we investigate the redshift distribution of the predictions of the bispectrum and compare them to those of

the power spectrum. We use the prediction coming from MODEL3.

The redshift contributions of the power spectrum are shown in Fig. 4. As the wavelength increases, the contribution of low to moderate redshift galaxies ($0 < z < 0.7$ and $0.7 < z < 1.5$) decreases while that of higher-redshift galaxies ($1.5 < z < 3$ and $z > 3$) increases. Fig. 5 and 6 show the redshift contributions of, respectively, the equilateral and squeezed bispectra. In both case, we do recover the same trend observed for the power spectrum. The relative contribution of high redshift galaxies gets larger as the wavelength increases while that of low-redshift galaxies decreases. However, bispectra at each wavelength and in both configurations are dominated by the contribution of galaxies at low redshift ($0 < z < 0.7$), which is due to a projection effect ($1/r^4(z)$ factor in Eq.2). This domination does not arise

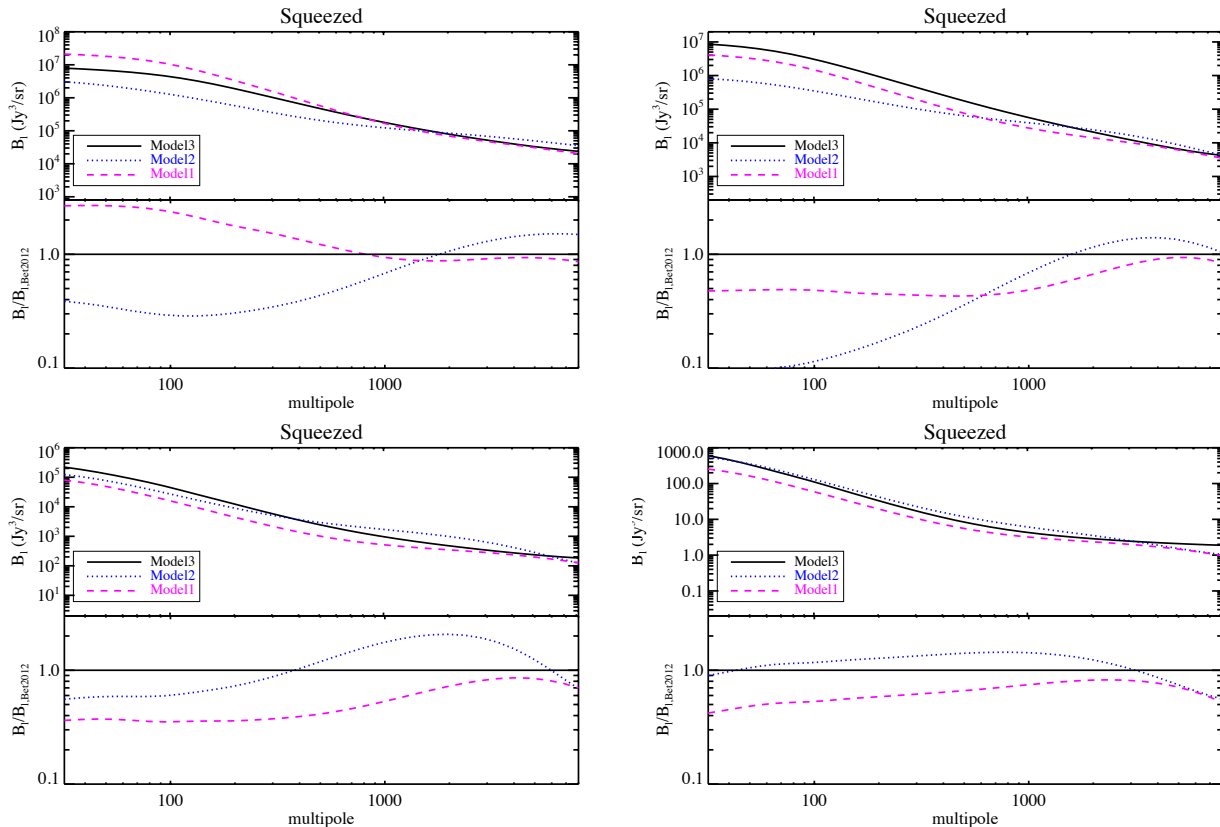


Figure 3. Top panels: squeezed bispectra computed with the three models of evolution of galaxies at long wavelengths. Low panels: ratios between MODEL2 and MODEL1 bispectra compared to the one computed with MODEL3.

on all scales, and the domination range depends on wavelength as well as configuration. Indeed, other redshift bins may dominate depending on scale wavelength and configuration. configuration galaxies with $0 < z < 0.7$ dominate up to $\ell \sim 300$. At higher multipoles, higher redshift galaxies dominate the bispectrum. The bin $0.7 < z < 1.5$ contributes the most at $350 \mu\text{m}$ while the contribution of the range $1.5 < z < 3$ increases with the wavelength and dominates the squeezed bispectrum at $\lambda \geq 850 \mu\text{m}$. Therefore it appears that the bispectrum will not give easily access to high redshift galaxies. Nevertheless, applying a flux cut to the emissivities is equivalent to removing low z sources (see Sect. 5).

4.2 Redshift and mass contributions simultaneously

We investigate the evolution of the mass contributions of each component with the redshift as shown in Fig. 8. To this end, we consider the equilateral configuration at the multipole $\ell = 1958$, $\ell = 133$, $\ell = 32$, and $\ell = 1958$ for the 1-halo, 2-halo, 3-halo, and shot-2galaxies terms respectively. Indeed, these are the multipoles where the respective terms are important.

The 1-halo term is dominated by galaxies hosted by high mass halos ($10^{14}M_{\odot} < M_{\text{halo}} < 10^{15}M_{\odot}$) at $z \sim 1$. As the redshift increases, the dominating mass range shifts towards lower halo mass, $\sim 10^{13}M_{\odot}$.

The 2-halo term is also dominated by galaxies that are in

halos of $10^{15}M_{\odot}$ but at lower redshift, $z \sim 0.5$. The dominating halo mass range shifts to lower mass with increasing redshift, up to $10^{13}M_{\odot}$ at $350 \mu\text{m}$ and up to $10^{11-12}M_{\odot}$ at $1380 \mu\text{m}$.

Concerning the 3-halo term, halos from a large mass range ($10^{12}M_{\odot} < M_{\text{halo}} < 10^{15}M_{\odot}$) as well as from a large redshift range ($0 < z < 2$) contribute equally at $350 \mu\text{m}$. As the redshift increases the mass range gets smaller and the dominating halo mass tends to $\sim 10^{13}M_{\odot}$. This trend is observed at the other wavelengths but the dominating mass at redshift higher than 2 gets even smaller, $10^{12}M_{\odot}$ at $1380 \mu\text{m}$. We can also notice that galaxies in halos with $10^{11}M_{\odot} < M_{\text{halo}} < 10^{14}M_{\odot}$ from redshift 0.5 to 3 contribute equally at $1380 \mu\text{m}$, while the mass range gets thinner towards high redshifts (and centered around $10^{12}M_{\odot}$). Indeed as the redshift increases the cut-off of the halo mass function goes to smaller halo masses.

Lastly, the 2-galaxies shot noise is dominated by galaxies in massive halos of $10^{14}M_{\odot} < M_{\text{halo}} < 10^{15}M_{\odot}$ at $350 \mu\text{m}$. As the wavelength gets longer, the redshift/mass domination spreads to higher redshifts and to an intermediate halo mass, $10^{12}M_{\odot}$ at $1380 \mu\text{m}$.

We do recover that higher redshift galaxies contribute relatively more at long wavelengths than at short ones and that each term is sensitive to a different mass range.

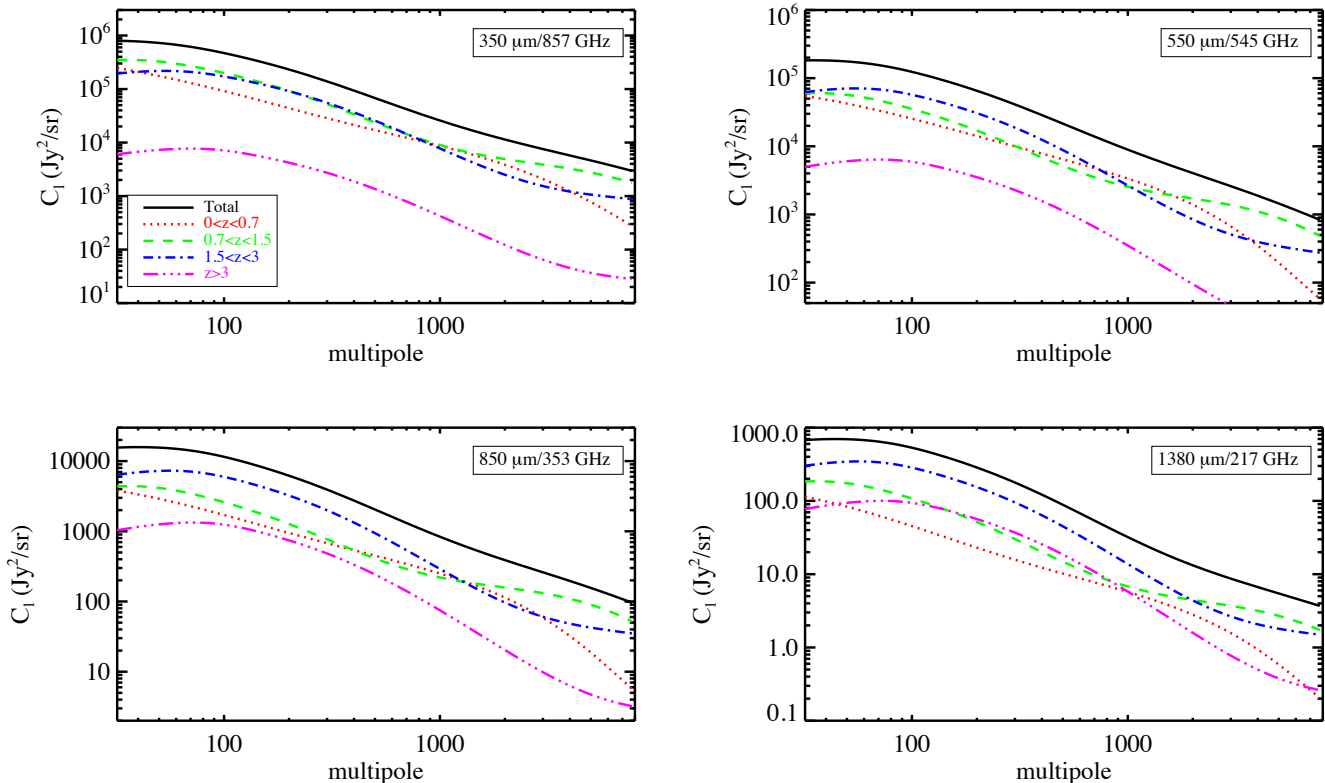


Figure 4. Redshift contributions of the power spectra coming from MODEL3.

5 THE IMPORTANCE OF THE EMISSIVITIES FLUX CUTS

When comparing CIB observations and models, one has to account for the so-called flux cut, that is the flux up to which galaxies are resolved as point sources and below which the IR emission is in form of unresolved anisotropies. This limit in flux depends on the resolution of the instrument and its sensitivity, thus on the level of confusion of the data as well as on the contamination of Galactic cirrus. Resolved point sources are most often masked for CIB studies and are mostly at low redshift, while the clustering is dominated by faint higher redshift sources which make the bulk of the anisotropies. The prediction of any statistics of the CIB, and in particular the power spectrum and the bispectrum, must hence account for the flux cut. It is straightforward to implement the flux cut in the mean emissivities, but one should also account for it in the 3D power spectrum/bispectrum as fewer galaxies are present in the map, particularly at low redshift. This effect must be taken into account in the HOD through the application of a redshift cut associated with the flux cut (see Paper1).

We consider here two sets of flux cuts, a conservative one as given in the ERCSC (Planck Collaboration et al. 2011b, Early Release Compact Source Catalogue of **Planck**) dedicated to CIB fields where there is not much contamination by Galactic cirrus (Planck Collaboration et al. 2011b) and an optimistic one as quoted in **Planck** Blue Book. Flux and associated redshift cuts are listed in Table 2. The cuts are applied to both the emissivity and the HOD.

Making use of MODEL3, we investigate how the bispectrum varies with the two sets of flux/redshift cuts. Fig. 9 shows the flux-cut emissivities as well as the limits in redshift we consider. The difference between the two sets of emissivities lies at low redshift, as expected. At $z = 0.01$, it reaches factors of 2.5 and 1.8 at 350 and 1380 μm , respectively. We can also note that the redshift range on which this difference applies decreases with the wavelength. Indeed, the contribution to the anisotropies of the CIB from low-redshift galaxies decreases with the wavelength (Fernandez-Conde et al. 2008). We then compare, for illustration, the equilateral bispectra derived with both sets of flux/redshift cuts as shown in Fig. 10. The squeezed bispectrum displays the same behaviour. The main difference between these bispectra lies at large angular scales, up to $\ell \sim 250$ at 350 μm and $\ell \sim 120$ at 1380 μm . The largest difference, up to a factor four, is between the two bispectra at 1380 μm . At the longest wavelength, we also note a difference at small angular scales, $\ell \geq 2000$, because of the 1-galaxy shot noise which is higher for the ERCSC flux cuts. Indeed the 1-galaxy shot noise depends strongly on the flux cut as shown in Eq. 16.

We examined each separate term of the bispectrum and found that these differences at large angular scale are mostly due to the 1-halo term which is the most sensitive to the redshift/flux cut, whereas the 2-halo and 2-galaxy shot noise terms are only slightly affected, displaying a variation of $\sim 5\%$ at large angular scales. We also investigated the separate effect of respectively the flux cut and the redshift cut on the bispectrum. Although both cuts have a noticeable effect, we found that the differences in Fig.10 are mainly due

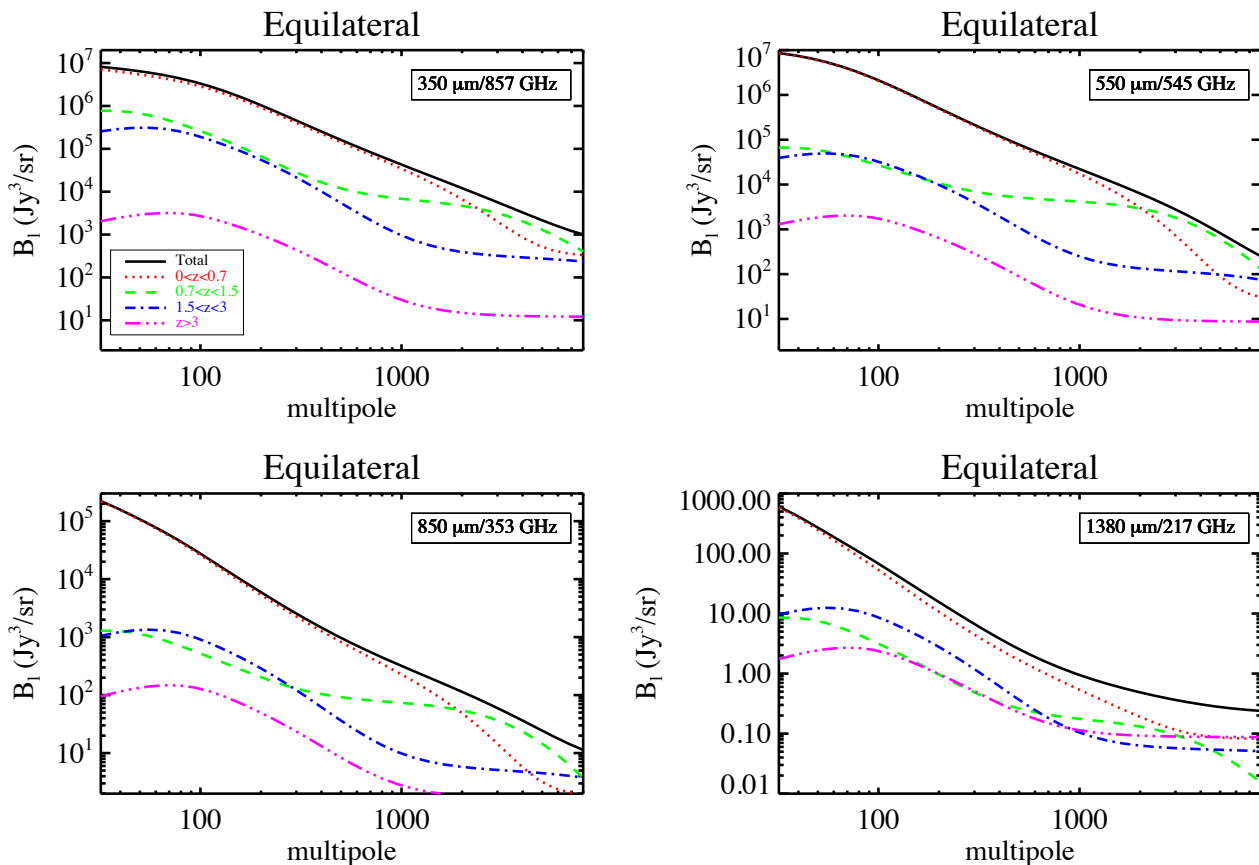


Figure 5. Redshift contributions of the equilateral bispectra coming from MODEL3.

Wavelength (μm)	Frequency (GHz)	S_{cut}^1 (mJy)	z_{cut}^1	S_{cut}^2 (mJy)	z_{cut}^2
350	857	813	0.03	300	0.04
550	545	471	0.02	180	0.03
850	353	249	0.01	75	0.02
1380	217	280	0.01	37	0.02

Table 2. The flux cuts and associated redshift cuts considered in the present study. S_{cut}^1 and z_{cut}^1 are given for the ERCSC 10σ flux cuts (Planck Collaboration et al. 2011b). S_{cut}^2 and z_{cut}^2 are the flux cuts at 3σ quoted in the Planck Blue Book.

to the flux cuts applied to the emissivities and not to the redshift cuts applied to the HOD.

We have seen in Sect. 4.1 that low redshift galaxies dominate the bispectrum at all wavelength. We investigate to which extent we can remove this contribution by applying a more drastic flux cut. Indeed instruments such as SPT and Herschel have higher resolutions that enable the application of lower flux cuts and thus the removal of more low redshift sources. We apply a flux cut of 50 mJy as used by Viero et al. (2012) for Herschel/SPIRE data. The relative contributions of each redshift bin only vary of a few percents at wavelengths longer than $550 \mu\text{m}$, however the situation strongly changes at $350 \mu\text{m}$ as shown in Fig. 7. This wavelength, compared to the others, is the most sensitive to low redshift and thus to the flux cut. A lower flux cut reduces the contribution of the low z range. For instance, at $\ell = 93$ for the equilateral configuration, the relative contribution of the slice $0 < z < 0.7$ drops from 87 % to 41 % while that at $0.7 < z < 1.5$ and $1.5 < z < 3$ increase from 8 % to 33%

and from 6 to 24 %, respectively. The highest redshift bin contributes to less than 1 % in both case. The application of a low flux cut limits the contribution of low redshift galaxies only at $350 \mu\text{m}$. At longer wavelength, the bispectrum keeps being dominated by these galaxies regardless of the flux cut.

6 CONTAMINATION OF THE CMB BISPECTRUM AND CONSTRAINING THE HOD PARAMETERS

Lacasa et al. (2012) studied the contamination of IR galaxies to the CMB bispectrum by computing the CIB anisotropies bispectrum with a prescription grounded on their power spectrum. They first showed that both the CMB and CIB bispectra are maximum in the squeezed configuration. Moreover, they estimated the contamination of the local CMB non-Gaussianity by computing the bias on f_{NL} induced by IR galaxies, Δf_{NL} . They showed that the IR galax-

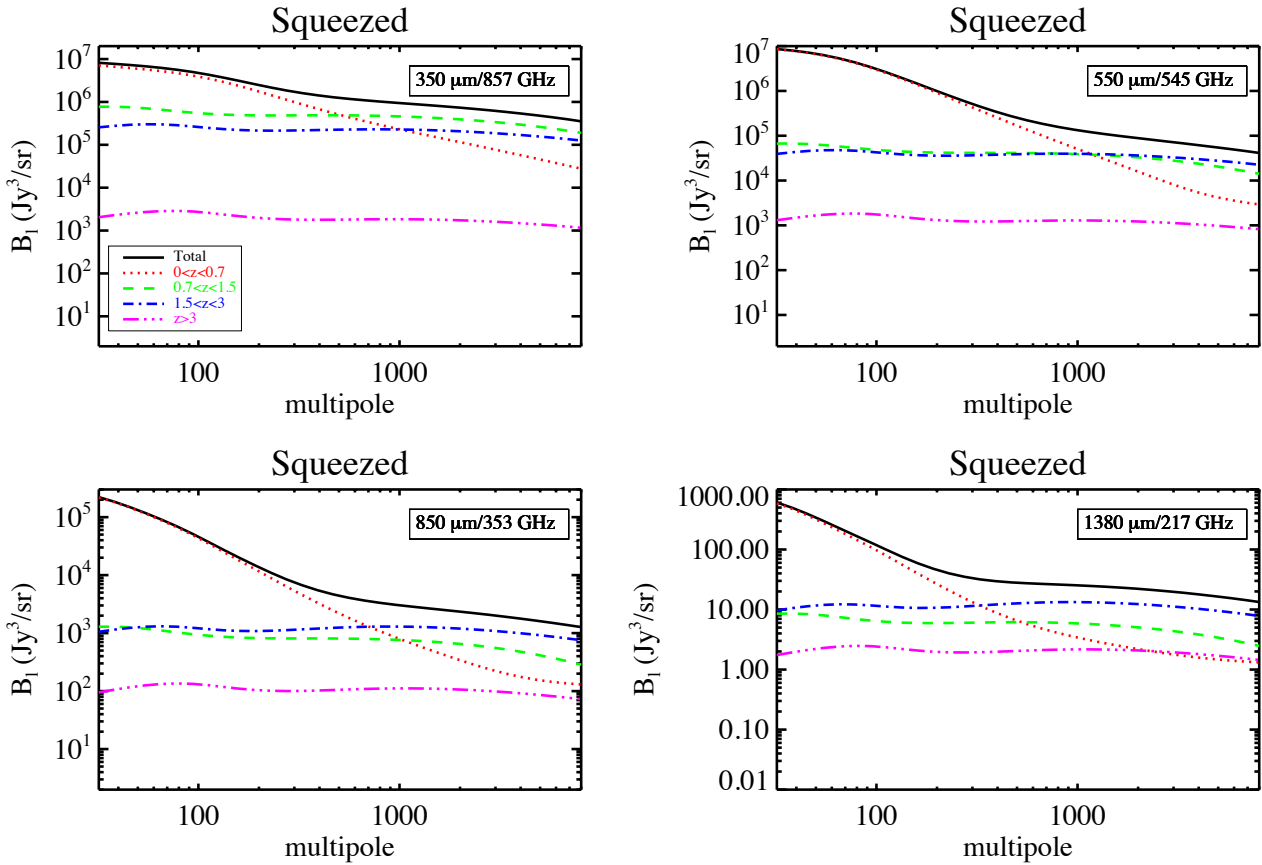


Figure 6. Redshift contributions of the squeezed bispectra coming from MODEL3.

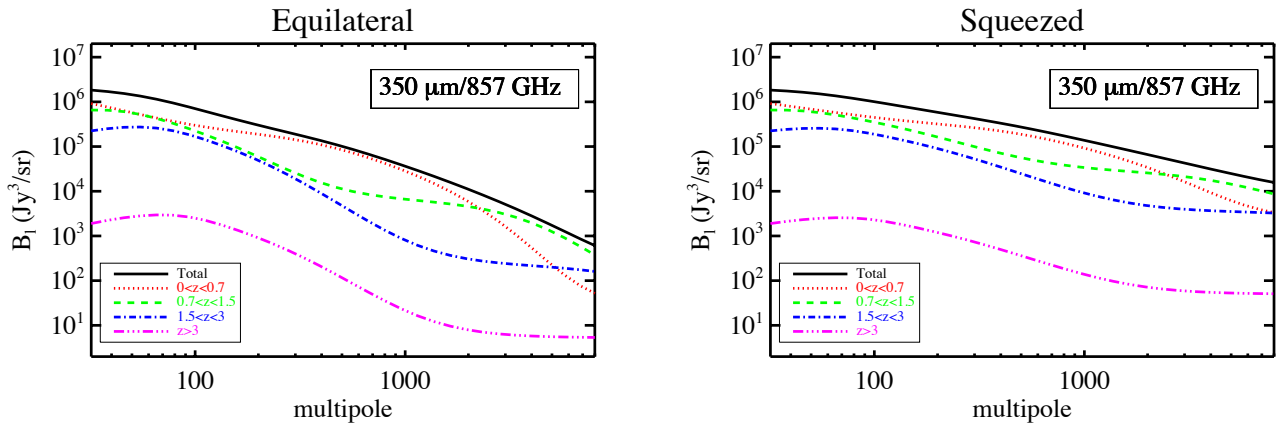


Figure 7. Redshift contributions of the equilateral and squeezed bispectra coming from MODEL3 with low flux cuts.

ies produce a negative bias which becomes important for *Planck*-like resolution and at low wavelengths. For instance, $\Delta f_{\text{NL}} \sim -6$ at $1380 \mu\text{m}$ and $\Delta f_{\text{NL}} \sim -60 - 70$ at $850 \mu\text{m}$. Most of the signal is due to the clustering of unresolved sources that make the CIB. Therefore they conclude that the bias Δf_{NL} is not reduced when applying a lower flux cut and, in some cases, it even increases because of the reduction of the shot noise term.

Here, we simply compare CIB and CMB bispectra at

Planck wavelengths. to this end, we assume primordial non-Gaussianity of the local type with $f_{\text{NL}} = 1$. Fig. 11 shows the comparison of the equilateral and squeezed bispectrum of the CMB to our predictions using the three models of galaxies investigated in the present study. We do not display the comparison at $350 \mu\text{m}$ as the CIB bispectrum dominates the CMB one by more than eight orders of magnitude. Concerning the equilateral configuration, the CIB bispectrum highly dominates that of the CMB at $550 \mu\text{m}$ as there

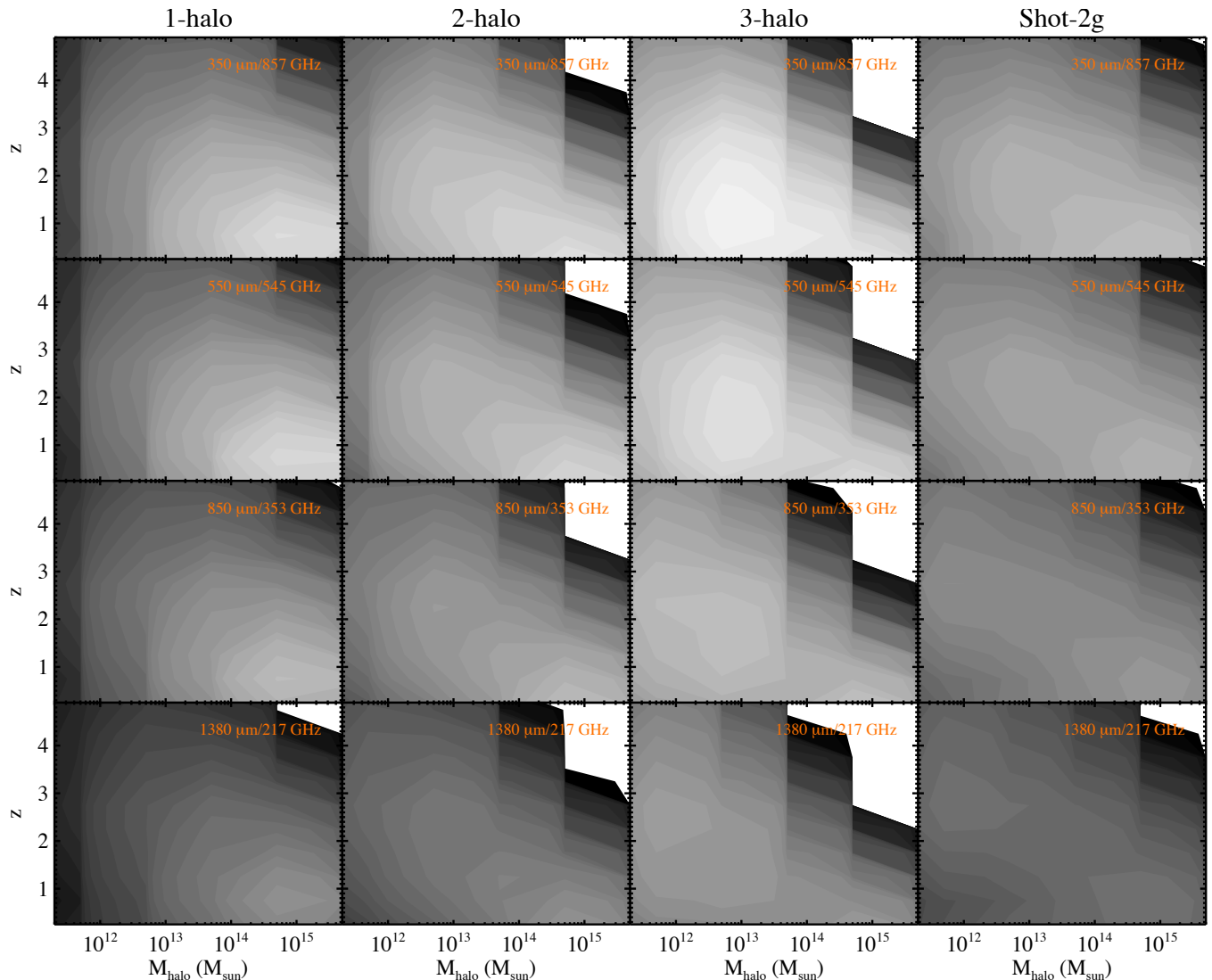


Figure 8. Halo mass contributions as a function of the redshift to the different terms of the equilateral bispectrum at several wavelengths. The light grey corresponds to the highest contribution. The step of color is logarithmic.

are 4 orders of magnitude between both. At longer wavelengths, the difference decreases and at $1380 \mu\text{m}$ both bispectra have similar amplitudes. The contamination of the CMB bispectrum by that of the CIB thus decreases with the wavelength. The situation changes with respect to the squeezed configuration. At $550 \mu\text{m}$, the CIB is still stronger by, at least, two orders of magnitude. At $850 \mu\text{m}$, the CMB bispectrum is slightly higher than that of the CIB and at $1380 \mu\text{m}$, the CIB bispectrum is dominated by that of the CMB by 3 orders of magnitude. In terms of CIB studies, the equilateral bispectrum is more appropriate to avoid the contamination by the CMB and we confirm that both CMB and CIB bispectra peak in the squeezed configuration.

A useful application to the measurement of the non-Gaussianity of CIB anisotropies is to constrain the HOD parameters. Pénin et al. (2012) showed, using several wavelengths simultaneously, that even if the HOD parameters are, on the whole, well constrained, M_{min} and M_{sat} are strongly degenerated. We carry a Fisher analysis to compare, first, how power spectra and bispectra measurements con-

strain HOD parameters alone and second, how the degeneracies are broken when combining both probes. We cannot use the four wavelengths together as the HOD parameters are different. Therefore we compute Fisher matrices for each wavelength using MODEL3 and assuming an optimistic fraction of the sky, 50%, over which spectra and bispectra are available. We bin both the power spectrum and the bispectrum, using 32 bins from $\ell = 32$ to $\ell = 2048$ with $\Delta\ell = 64$. We set ℓ_b the mean multipole over a bin. The Fisher matrix of the power spectrum is:

$$F_{ij}^{C_{\ell_b}} = \sum_{\ell_b} \frac{1}{\sigma_{\ell_b, C_{\ell_b}}^2} \frac{dC_{\ell_b}}{d\theta_i} \frac{dC_{\ell_b}}{d\theta_j} f_{\text{sky}} \quad (25)$$

where θ_k is the k -th parameter and $\sigma_{\ell_b, C_{\ell_b}}$ is the error bar accounting for cosmic variance and instrumental noise:

$$\sigma_{\ell, C_{\ell_b}} = (C_{\ell_b} B_{\ell_b}^2 + N_{\ell_b}) \sqrt{\frac{2}{(2\ell_b + 1)\Delta\ell}} \quad (26)$$

Here N_{ℓ} is the level of the instrumental noise (Planck Col-

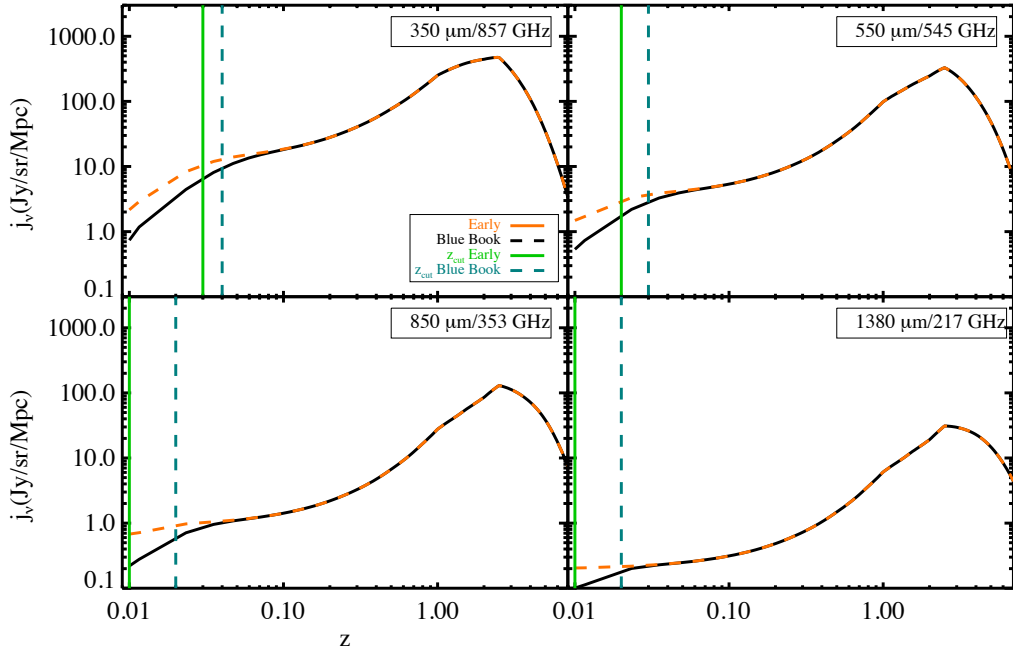


Figure 9. Emissivities of MODEL3 to which flux cuts have been applied. The vertical lines show the redshift cuts. These are illustrated both for ERCSC (orange) and Planck Blue Book (black) flux cuts.

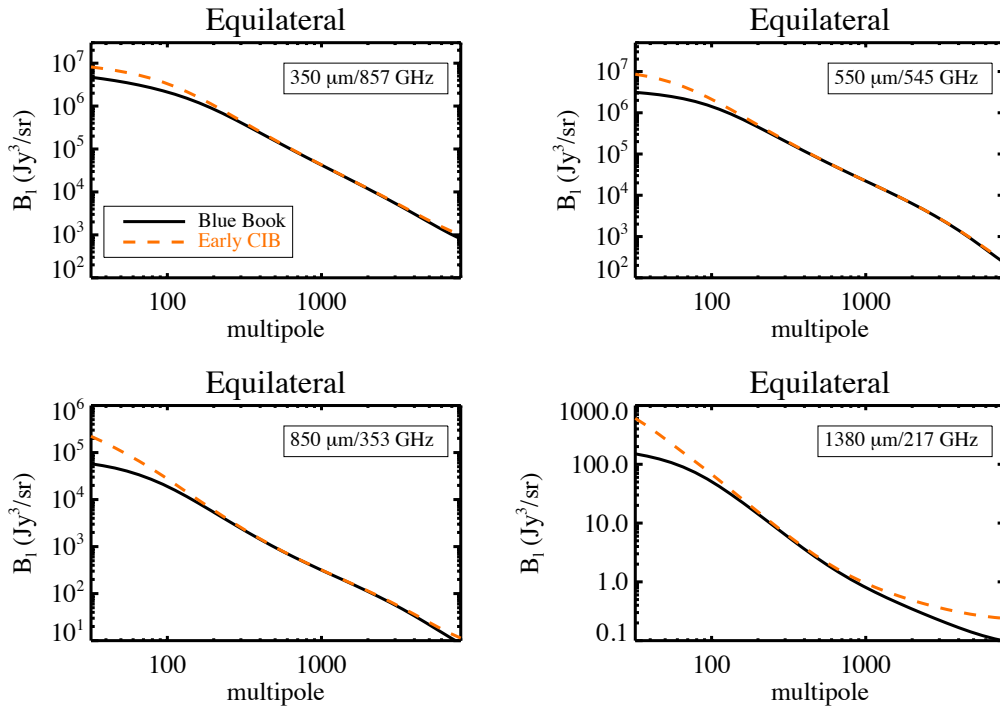


Figure 10. Equilateral bispectra computed using the two sets of flux cuts. The black and orange lines are the bispectra computed with Planck Blue Book and with the ERCSC flux cuts, respectively.

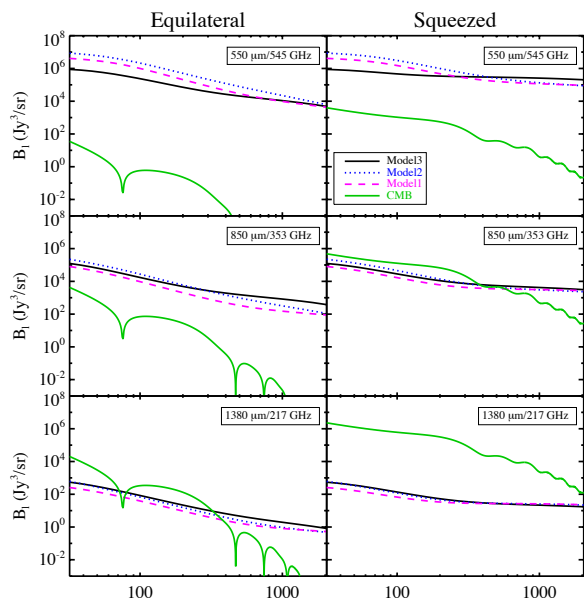


Figure 11. Equilateral and squeezed bispectra of DSFG compared to the CMB bispectrum (green).

laboration et al. 2011a), B_ℓ^2 the power spectrum of the point spread function and f_{sky} is the sky fraction.

The computation of the Fisher matrix is slightly different for the bispectrum. Indeed one needs to compute the full covariance matrix on all the possible configurations of the bispectrum $\text{Cov}(b_{\ell_1\ell_2\ell_3}, b'_{\ell_1\ell_2\ell_3})$ to compute the associated Fisher matrix. This covariance matrix contains Gaussian and non-Gaussian contributions :

$$\text{Cov}(b_{\ell_1\ell_2\ell_3}, b'_{\ell_1\ell_2\ell_3}) = \text{Cov}_G + \text{Cov}_{\text{NG}} \quad (27)$$

with the Gaussian contribution being diagonal and leading to an error contribution $\sigma_{\ell_1\ell_2\ell_3}$:

$$\sigma_{\ell_1\ell_2\ell_3}^2 = (C_{\ell_1} B_{\ell_1}^2 + N_{\ell_1})(C_{\ell_2} B_{\ell_2}^2 + N_{\ell_2})(C_{\ell_3} B_{\ell_3}^2 + N_{\ell_3}) \times \frac{1}{N_{\text{tri}}(\ell_1, \ell_2, \ell_3)} \quad (28)$$

where $N_{\text{tri}}(\ell_1, \ell_2, \ell_3)$ is the number of possible configurations of the triplet (ℓ_1, ℓ_2, ℓ_3) .

The non-Gaussian contribution to the covariance matrix is :

$$\begin{aligned} \text{Cov}_{\text{NG}}(b_{\ell_1\ell_2\ell_3}, b'_{\ell_1\ell_2\ell_3}) &= \frac{1}{\Delta\ell} b_{\ell_1\ell_2\ell_3} b'_{\ell_1\ell_2\ell_3} B_{\ell_1} B_{\ell_2} B_{\ell_3} B'_{\ell_1} B'_{\ell_2} B'_{\ell_3} \\ &\times \left[\frac{\delta_{\ell_1\ell'_1}}{2\ell_1+1} + \frac{\delta_{\ell_1\ell'_2}}{2\ell_1+1} + \frac{\delta_{\ell_1\ell'_3}}{2\ell_1+1} \right. \\ &+ \frac{\delta_{\ell_2\ell'_1}}{2\ell_2+1} + \frac{\delta_{\ell_2\ell'_2}}{2\ell_2+1} + \frac{\delta_{\ell_2\ell'_3}}{2\ell_2+1} \\ &\left. + \frac{\delta_{\ell_3\ell'_1}}{2\ell_3+1} + \frac{\delta_{\ell_3\ell'_2}}{2\ell_3+1} + \frac{\delta_{\ell_3\ell'_3}}{2\ell_3+1} \right] \quad (29) \end{aligned}$$

The Fisher matrix is then

$$F_{ij}^{b\ell} = {}^t X_{\theta_i} \text{Cov}(b_{\ell_1\ell_2\ell_3}, b'_{\ell_1\ell_2\ell_3})^{-1} X_{\theta_j} f_{\text{sky}} \quad (30)$$

where X_{θ_k} is the vector that contains the derivatives of the bispectrum with respect to the parameter θ_k .

We consider two cases. First, an ideal case, we assume no foreground residuals in the measurement of the CIB anisotropy power spectra and bispectra. Only instrumental

noise is added to the CIB measurements. Second, we consider a more realistic case in which contributions from CMB and dust residuals are also included to the power spectra and bispectra.

The upper panels of Fig. 12 show confidence ellipses at 350 and 1380 μm derived from the power spectrum (light blue), the bispectrum (orange), and the combination of both (black) for the ideal case. At 350 μm , the constraints induced by the bispectrum are tighter than those from the spectrum. Indeed, the bispectrum is much more sensitive to the variations of the HOD parameters than the power spectrum as shown in Paper1. In addition, the directions of degeneracy for the pairs $(\alpha_{\text{sat}}, M_{\text{min}})$ and $(\alpha_{\text{sat}}, M_{\text{sat}})$ leading to a break of the degeneracies and to a significant improvement of the accuracy when combining both data sets. The situation is different for the pair $(M_{\text{min}}, M_{\text{sat}})$ for which the directions of degeneracy from both the power spectrum and the bispectrum are the same. The improvement in the constraints on this pair of parameters is mostly driven by the higher sensitivity of the bispectrum to mass. At 1380 μm , degeneracies are broken for the three pairs of parameters leading to significantly improved constraints on the HOD parameters. For instance, 1σ error bars on α_{sat} given by C_ℓ and b_ℓ alone are poor, $\sim 500\%$ and $\sim 100\%$, respectively. It is reduced to $\sim 50\%$ when power spectrum and bispectrum are combined. Note that the large errors bars at long wavelengths are due to instrumental noise.

A more realistic case is to consider residuals of foregrounds in the measured power spectra and bispectra. Following Planck Collaboration et al. (2013a), we assume 10 % contamination by the CMB to the CIB power spectrum and we discard from the analysis low multipoles where Galactic dust has a non-negligible contribution to the power spectrum and to the bispectrum. We assume a null non-Gaussianity as f_{NL} has been shown to be close to zero (Planck Collaboration et al. 2013b). The lower panels of Fig. 12 show the confidence ellipses at 350 and 1380 μm including foreground residuals. Parameters constraints are, of course, poorer for both bispectra and power spectra. Nevertheless the orthogonality of the directions of degeneracy is preserved significantly leading to improved constraints, still poorer than the ideal case. For instance, at 350 μm the 1σ error bar on α_{sat} given by the combination of both data sets is 12% in the ideal case and increases to 49% when including foreground residuals. The situation is similar at 550 and 850 μm however, at 1380 μm the constraints are highly worsened because the CMB is dominant at that wavelength.. The 1σ error bar on α_{sat} rises from 55 to 220 % from the ideal to the realistic case.

The constraints on the HOD parameters heavily depend on the fraction of sky available for the measurement of both power spectrum and bispectrum. This is illustrated by varying the sky fraction from 10% to a very optimistic case of 70% of sky. Changing f_{sky} does not change the degeneracy directions, only the error bars on the parameters, which scale as $\propto \sqrt{f_{\text{sky}}}$. These error bars are listed in Table 3 as percentages of the fiducial HOD parameter values for each wavelength and for both ideal and realistic cases. The slope of the number of satellites, α_{sat} is the most affected by the addition of foreground residuals, error bars get poorer by a factor ~ 5 at most. The error bars on M_{min} and M_{sat} are also

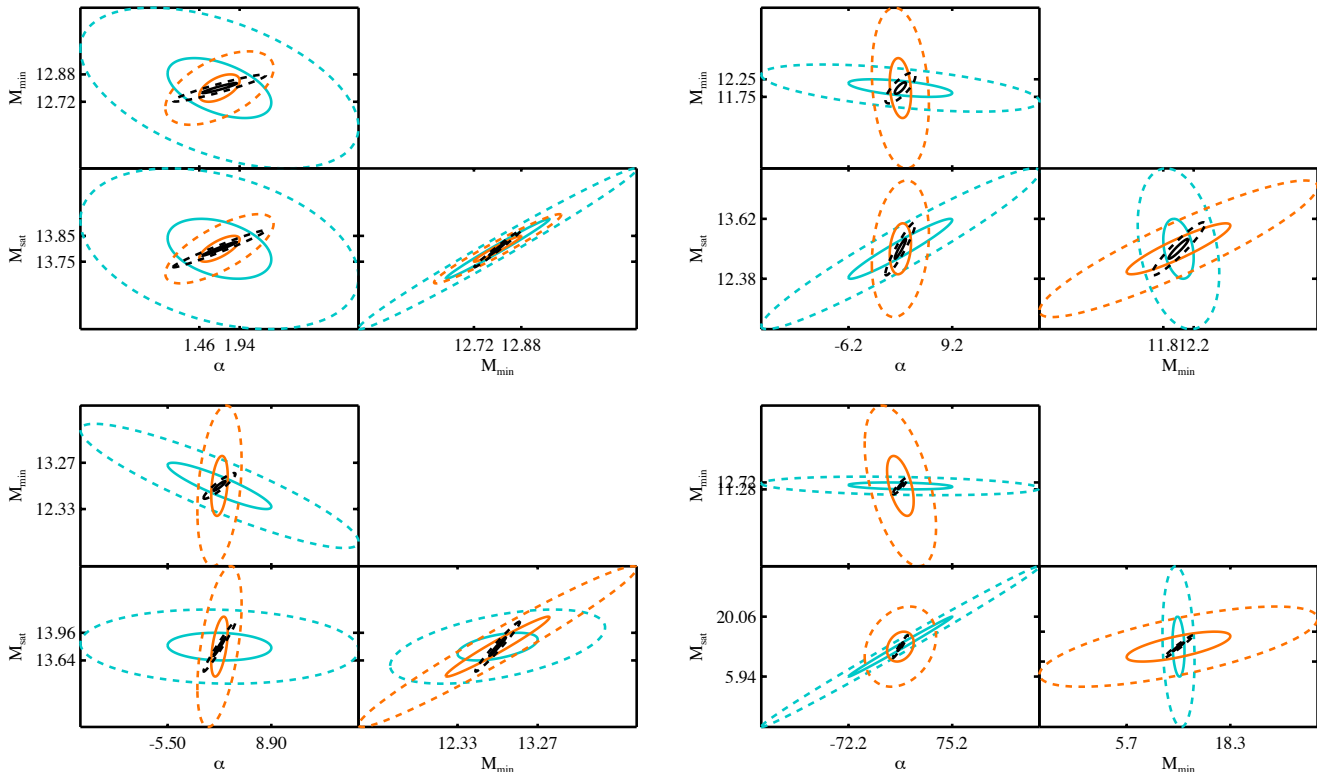


Figure 12. Confidence ellipses for HOD parameters coming from the power spectrum (light blue), the bispectrum (orange) and the combination of both (black) at 350 and 1380 μm on the left and right panels, respectively. Top panels are for the ideal case with only instrumental noise added to the measurements while lower panels are for the realistic case that includes foregrounds residuals. Solid lines are the confidence ellipses at 1σ and the dashed lines are those at 2σ .

affected, by a factor ~ 3 at most, but they remain excellent. In both cases, the small error bars on M_{min} and M_{sat} are striking, at the maximum of order of few percents up to 850 μm . This comes from the orthogonality of the directions of the degeneracies from C_ℓ and b_ℓ . Constraints at 1380 μm are highly worsened when adding foregrounds residuals because of the high amplitude of the CMB at this wavelength. We also note that 50% of the sky is sufficient to constrain accurately the HOD parameters.

7 CONCLUSION

We have presented a model of the bispectrum of unresolved dusty star-forming galaxies in the Cosmic Infrared Background. It is developed in the framework of the halo model and a halo occupation distribution interfaced with a model of evolution of galaxies. We have predicted bispectra of the CIB anisotropies at *Planck* wavelengths for three recent models of evolution of galaxies. Interestingly, these models do not predict the same amount of non-Gaussianity.

Surprisingly, regardless of the wavelength, bispectra are dominated by low redshift galaxies ($z < 0.7$) whereas it is not the case for the power spectrum. Indeed, for the latter, the contributions of low redshift galaxies decreases as the wavelength gets longer while the contribution of higher redshift galaxies increases. Nevertheless, even if bispectra are dominated by low redshift galaxies, we still recover the trend observed for the power spectrum below

that dominant contribution. This strong contribution of the low redshift bin galaxies is due to the 2D projection of the 3D bispectrum. In order to take into account the flux cut applied to CIB maps for the removal of resolved point sources, we introduced a redshift cut in the HOD. By applying a very low flux cut, for instance one typical of *Herschel* or SPT, we are not able to remove a large fraction of the contamination of low redshift galaxies and thus access to the contribution from higher redshift galaxies.

We have investigated the mass and redshift dependence of each term of the bispectrum and as a function of the wavelength. We do recover similar results to the power spectrum case. The four terms of the bispectrum that depend on the HOD do not have the same mass dependence. For instance, the 1-halo term is dominated by high mass halos up to a redshift of 3 whereas the main contribution to the 2-halo term is from high mass halos at low redshift and the dominating mass shifts to intermediate halo masses at higher redshifts. The contribution of the 3-halo term is mainly due to galaxies that lie in intermediate mass halos in the redshift range $z = [0, 4]$.

We compare our predictions of the bispectrum of CIB anisotropies to the bispectrum of the CMB in the case of $f_{\text{NL}}=1$. We do confirm that both bispectra are maximum in the squeezed configuration. It might be complex to disentangle between them at wavelengths longer than 850 μm if the CMB cannot be removed properly.

The clustering part of the galaxy model is fully parametric

Wavelength μm	Frequency GHz	Ideal case				Realistic case		
		f_{sky}	α_{sat}	$\log M_{\text{min}}$	$\log M_{\text{sat}}$	α_{sat}	$\log M_{\text{min}}$	$\log M_{\text{sat}}$
350	857	10%	27.3%	0.5%	0.5%	109%	1.7%	1.8%
		30%	15.7%	0.3%	0.3%	63%	1%	1%
		50%	12.2%	0.2%	0.2%	49%	0.8%	0.8%
		70%	10.3%	0.2%	0.2%	41%	0.6%	0.7%
550	545	10%	10.3%	0.3%	0.2%	50%	1.3%	1.2%
		30%	6.0%	0.2%	0.1%	29%	0.7%	0.7%
		50%	4.6%	0.1%	0.1%	22%	0.6%	0.5%
		70%	3.9%	0.1%	0.1%	19%	0.5%	0.4%
850	353	10%	22.7%	0.9%	0.8%	72%	2.4%	2.4%
		30%	13.1%	0.5%	0.4%	42%	1.4%	1.4%
		50%	10.2%	0.4%	0.3%	32%	1%	1%
		70%	8.6%	0.3%	0.3%	27%	0.9%	0.9%
1380	217	10%	123.7%	3.0%	3.5%	582%	12%	17%
		30%	71.4%	1.7%	2.0%	337%	7%	10%
		50%	55.3%	1.3%	1.6%	260%	5%	8%
		70%	46.7%	1.1%	1.3%	220%	5%	7%

Table 3. 1σ error bars on the HOD parameters when combining power spectrum and bispectrum data as a function of the available sky fraction at different wavelengths in both the ideal and realistic cases. The fiducial values of the HOD parameters are listed in Table 1.

which enables us to carry a Fisher analysis to investigate to which extent the model parameters are constrained with the power spectrum, bispectrum alone and when combining both. We consider one ideal case including only the CIB and the instrumental noise and a more realistic case in which foreground residuals are added. In both cases, when combining both data sets, directions of degeneracy of C_ℓ and b_ℓ are usually orthogonal which improves significantly the constraints on the HOD parameters. We show that C_ℓ and b_ℓ measurements over a fraction of the sky of 50% provides between 0.2 % and 10 % error bars on the HOD parameters in the ideal case and between 0.5 and 50 % for the realistic case up to 850 μm .

ACKNOWLEDGMENTS

The authors thank B. Béthermin for useful discussions and for providing us the emissivities from Béthermin et al. (2012a). The authors also wish to acknowledge our referee S. Prunet, G. P. Holder, C. Porciani, C. Schimd, E. Sefusatti, G. Lagache, J. Tinker, and A. Wetzel for useful discussions and M. Langer for a thorough reading of the manuscript.

REFERENCES

- Amblard A. et al., 2011, *Nature*, 470, 510
 Argüeso F., González-Nuevo J., Toffolatti L., 2003, *ApJ*, 598, 86
 Bennett C. L. et al., 2003, *ApJ*, 583, 1
 Berlind A. A., Weinberg D. H., 2002, *ApJ*, 575, 587
 Béthermin M. et al., 2012a, *ApJ*, 757, L23
 Béthermin M., Dole H., Lagache G., Le Borgne D., Penin A., 2011, *A&A*, 529, A4+
 Béthermin M. et al., 2012b, *A&A*, 542, A58
 Bouwens R. J. et al., 2012, *ApJ*, 754, 83
 Bouwens R. J. et al., 2011, *ApJ*, 737, 90
 Cooray A. et al., 2010, *A&A*, 518, L22+
 Cooray A., Sheth R., 2002, *Physics Reports*, 372, 1
 Coupon J. et al., 2012, *A&A*, 542, A5
 Crawford T. M. et al., 2013, *ArXiv e-prints*
 Croton D. J. et al., 2006, *MNRAS*, 365, 11
 Fernandez-Conde N., Lagache G., Puget J.-L., Dole H., 2008, *A&A*, 481, 885
 Fowler J. W., Atacama Cosmology Telescope Team 2010, in *Bulletin of the American Astronomical Society*. pp 599–+
 Fry J. N., 1984, *ApJ*, 277, L5
 Gao L., White S. D. M., Jenkins A., Stoehr F., Springel V., 2004, *MNRAS*, 355, 819
 Gil-Marín H., Wagner C., Fragkoudi F., Jimenez R., Verde L., 2012, *JCAP*, 2, 47
 Gruppioni C., Pozzi F., Zamorani G., Vignali C., 2011, *MNRAS*, 416, 70
 Haiman Z., Knox L., 2000, *ApJ*, 530, 124
 Hall N. R. et al., 2010, *ApJ*, 718, 632
 Jauzac M. et al., 2011, *A&A*, 525, A52+
 Knox L., Cooray A., Eisenstein D., Haiman Z., 2001, *ApJ*, 550, 7
 Komatsu E. et al., 2003, *Astrophysical Journal Supplement Series*, 148, 119
 Kravtsov A. V., Berlind A. A., Wechsler R. H., Klypin A. A., Gottlöber S., Allgood B., Primack J. R., 2004, *ApJ*, 609, 35
 Lacasa F., Aghanim N., Kunz M., Frommert M., 2012, *MNRAS*, 421, 1982
 Lacasa F., Pénin A. A., Aghanim N., 2013, accepted by *MNRAS*
 Lagache G., Bavouzet N., Fernandez-Conde N., Ponthieu N., Rodet T., Dole H., Miville-Deschênes M.-A., Puget J.-L., 2007, *ApJ*, 665, L89
 Lagache G. et al., 2004, *Astrophysical Journal Supplement Series*, 154, 112
 Lagache G., Puget J. L., 2000, *A&A*, 355, 17
 Lapi A. et al., 2011, *ApJ*, 742, 24
 Navarro J. F., Frenk C. S., White S. D. M., 1996, *ApJ*, 462, 563
 Negrello M., Perrotta F., González-Nuevo J., Silva L., de Zotti G., Granato G. L., Baccigalupi C., Danese L., 2007,

- MNRAS, 377, 1557
Oliver S. J. et al., 2010, A&A, 518, L21+
Pénin A., Doré O., Lagache G., Béthermin M., 2012, A&A, 537, A137
Pénin A. et al., 2012, A&A, 543, A123
Planck Collaboration et al., 2013b, ArXiv e-prints
Planck Collaboration et al., 2013a, ArXiv e-prints
Planck Collaboration et al., 2011b, A&A, 536, A7
Planck Collaboration et al., 2011a, A&A, 536, A18
Sargent M. T., Béthermin M., Daddi E., Elbaz D., 2012, ApJ, 747, L31
Sheth R. K., Tormen G., 1999, MNRAS, 308, 119
Tinker J., Kravtsov A. V., Klypin A., Abazajian K., Warren M., Yepes G., Gottlöber S., Holz D. E., 2008, ApJ, 688, 709
Tinker J. L., Wechsler R. H., Zheng Z., 2010, ApJ, 709, 67
Tinker J. L., Wetzel A. R., 2010, ApJ, 719, 88
van den Bosch F. C. et al., 2007, MNRAS, 376, 841
Viero M. P. et al., 2009, ApJ, 707, 1766
Viero M. P. et al., 2012, ArXiv e-prints
Xia J.-Q., Negrello M., Lapi A., De Zotti G., Danese L., Viel M., 2012, MNRAS, 422, 1324
Zheng Z. et al., 2005, ApJ, 633, 791